Development of an Innovative Procedure for Lithium Plating Limitation and Characterization of 18650 Cycle Aged Cells for DCFC Automotive Applications

Matteo Dotoli [1,2,*], **Emanuele Milo** [3,*], **Mattia Giuliano** [2], **Arianna Tiozzo** [1,2], **Marcello Baricco** [1], **Carlo Nervi** [1], **Massimiliano Ercole** [3] and **Mauro Francesco Sgroi** [1,*]

1   Materials & Sustainaibility Engineering South Europe Technical Center, Centro Ricerche Fiat S.C.p.A, Orbassano, 10043 Turin, Italy
2   Department of Chemistry, NIS–INSTM–University of Turin, 10125 Turin, Italy
3   Propulsion Systems, South Europe Packs Integration, FCA Italy SPA, 10135 Turin, Italy
*   Correspondence: matteo.dotoli@unito.it (M.D.); emanuele.milo@stellantis.com (E.M.); mauro.sgroi@crf.it (M.F.S.)

Abstract: Since lithium-ion batteries seem to be the most eligible technology to store energy for e-mobility applications, it is fundamental to focus attention on kilometric ranges and charging times. The optimization of the charging step can provide the appropriate tradeoff between time saving and preserving cell performance over the life cycle. The implementation of new multistage constant current profiles and related performances after 1000 cycles are presented and compared with respect to a reference profile. A physicochemical (SEM, XRD, particle size analysis, etc.) and electrochemical (incremental capacity analysis, internal resistance measurements) characterization of the aged cells is shown and their possible implementation on board is discussed.

Keywords: lithium plating; fast charging; automotive; electric vehicles; li-ion battery; MCC; cutoff voltage; cycle aging; postmortem characterization

1. Introduction

In a wide panorama with several new emerging energy storage approaches [1–6] to guide the ecological transition, today lithium-ion batteries are considered among the most promising and mature technologies [7], with an increasing interest coming from the main players in the automotive field. Carmakers are always more and more pushed by governments to switch their fleets from internal combustion engines (ICEs) to hybrid and electric powertrains, with strict deadlines [8,9] and carbon neutrality targets by 2035.

Lithium-ion cells, showing significant energy (150–200 Wh/Kg) and power (300–1500 W/Kg) densities along with affordable durability, seem to cover a key role to trace this route [10]. One of the main topics the researchers are dealing with is related to the implementation of optimized fast charging profiles to decrease charging time and to limit cell degradation, maintaining performances and reducing capacity fade [11]. Among the wide panorama of charging approaches, multistage constant current charging (MCC) represents a good compromise between efficiency and easy implementation for a battery management system (BMS) [12].

Indeed, when working with lithium-ion cells, degradation inside the active materials is inevitable and directly affected by stress factors, such as high depth of discharge (DoD), high charging-rates, and low temperatures. During the life cycle of a lithium-ion cell, aging affects the performances of the electrochemical system, with the risk of also compromising safety [13,14].

Aging detection is challenging because of the interdependency of plenty of complex sets of degradation mechanisms, bringing capacity and power fade with chemical and

mechanical origins. Among the most widespread aging effects, literature [15–18] widely reports the loss of lithium inventory (LLI) as a main route cause for lithium loss. This is mainly attributed to the formation of a continuous solid electrolyte interphase (SEI), caused by the occurrence of parasitic reactions.

The loss of active material (LAM) is mainly due to mechanical and structural degradations of the electrode, with no direct evidence in terms of the capacity fade. Ohmic resistance increase (ORI) is then referred to electrodes and electrolyte degradation. Lithium plating is considered among the most dangerous aging effects occurring in lithium ion cells, since it causes safety issues and fast capacity decay [19–21].

It is reported that, among cycling aging effects, SEI formation and LAM are generally described by a linear aging trend [22]. The incoming of the "knee point" (inflection point) in the curve of state of health (SoH) vs. n° cycles is often linked to the onset of irreversible lithium plating [23,24].

Since these processes take place simultaneously, it is very difficult to identify each single aging contribution. To better understand the aging conditions, it is useful to match "in-situ" electrochemical techniques with an extensive post-mortem analysis [25–27].

In this contest "in-situ" methodologies are revealed to be suitable and versatile for their use in on-board applications and on BMS, along with their advantage of being non-invasive. Among the most used techniques during cycle aging, we can cite incremental capacity analysis (ICA) [28,29] and internal resistance evaluation [30]. This work presents data obtained from a 1000 cycle aging campaign performed by charging cells with custom designed DCFC profiles. Electrochemical and physicochemical results are shown.

2. Materials and Methods

2.1. Battery Cells

Commercial 18650 cylindrical high energy density (215 Wh/Kg) cells were used. The active cathodic material was NMC811, the anodic material was Silicon-Graphite (Si-C), with an amount of silicon of 2 wt%. Both electrodes are double side coated. A mixture of EC:DMC (1:1), 1M LiPF$_6$ was used as electrolyte. Details about the cell are reported in previous papers [11,31].

2.2. Cycling Condition and Experimental Setup

2.2.1. Testing Facilities

The aging campaign was performed at 25 °C in a Falc climatic chamber, monitored by a Eurotherm controller (Como, Italy). Cells have been cycled with a BasyTec XCTS, controlled by BasyTec software (Asselfingen, Germany) (6.2.42.0 version).

2.2.2. Electrochemical Testing

Each cell was aged with a specific direct current fast charging (DCFC) profile, as reported in Figure 1, replicating the aging procedure defined in a previous study [11]. For this specific test, the end of life (EOL) was reached at 1000 cycles. The aim of this test was to try to limit lithium plating formation. The discharging step was chosen at 1C for all the cells, from 4.09 to 2.98 V.

Every 50 cycles, a capacity check was performed to control the aging trend. The capacity check consisted of two C/5 charge/discharge cycles between 2.50 V and 4.20 V.

A very slow charge/discharge (C/50) was performed before starting the aging protocol, to calculate the incremental capacity analysis (ICA) in quasi-stationary conditions. The same test was repeated for comparison at 1000 cycle (i.e., at the end of the aging campaign).
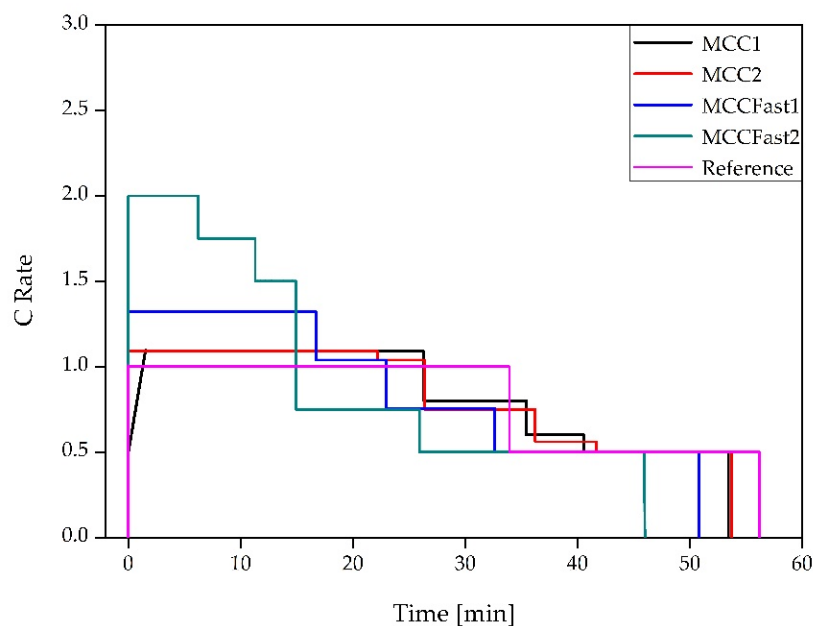
Figure 1. DCFC profiles.

2.2.3. Incremental Capacity Analysis

As widely reported in the literature [32–34], ICA consists in the calculation of the derivative dQ/dV, displayed as a function of the operative voltage. Considering observed peaks into a typical ICA plot (Figure 2—right side), we focused attention on the main transition phase during charge and discharge [32,33,35]. In fact, when the voltage profile curve (Figure 2—left side) shows a small slope, with a limited increase of the cell potential, a transition phase in both electrodes is occurring (i.e., H_1-M, M-H_2 etc.). More details will be provided in Section 4.2. Here, the voltage response profile is shown as a function of the state of discharge (SoD%).
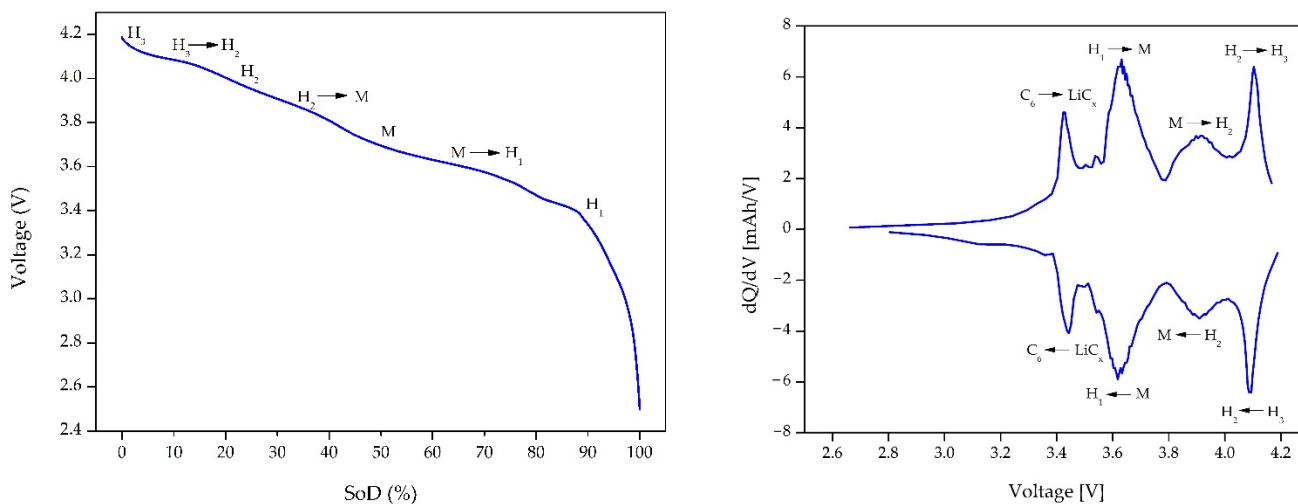

Figure 2. Example of ICA plots: (**left** side) (V vs. SoD%); (**right** side) (dQ/dV vs. V).

2.3. Teardown and Sampling

The post-mortem characterization of the electrodes was performed through the dismantling of the cells. To operate in safe conditions, the cells were discharged to 2.2 V and opened in an Ar-filled MBraun glovebox (<0.1 ppm O_2, <0.1 ppm H_2O).

The so-called "jellyroll", with a cylindrical shape, was composed by the staking of the anode and the cathode, separated by a polymeric foil. It was extracted from the aluminum external can, using a cutting tool (Dremel®) (Mount Prospect, USA) and unwounded.

The electrode samples were prepared inside the glovebox using a disk puncher (18 mm diameter), suitable for all the performed analyses. To increase the sampling statistics, it was decided to cut 10 electrode disks all over the original electrode foil surface, only where the electrode surface appears in good health on visual inspection. The samples were preserved in a specific box and selected randomly for all the electrochemical and XRD analyses.

2.4. XRD Analysis

XRD measurements were performed with a Rigaku Miniflex. Patterns were recorded with a Bragg-Brentano flat geometry, using a Cu-Kα radiation (λ = 1.5406 Å; 40 kV, 15 mA) at 0.02° interval in the range $5° < 2θ < 90°$ using a scanning velocity of 1°/min.

Cathode and anode active materials were tested in multiple conditions. Samples powders scratched from the electrode foil were analyzed, using the standard full scale sample holder. Calendered samples picked up from the electrode foils in the original format were characterized in inert atmosphere, employing a specific XRD sample holder with a Kapton window. Both the powder samples (obtained by machining a significant amount of material) and the surface conditions (limited only to the material in contact with the separator on the calendered electrode) were objects of study.

A Rietveld refinement was performed on XRD patterns using PDF software in the $15° < 2θ < 90°$ range, considering a single-phase system composed by NMC811, together with a small fraction of carbon phase, associated to the conductive agent present in the electrode formulation. A trigonal structure (s.g.: $R\bar{3}m$, 166) was assumed for the NMC811 phase as a model for the refinement.

2.5. SEM/EDX

SEM/EDX analyses were performed on a Zeiss Sigma Scanning Electron Microscope (Oberkochen, Germany) (SEM) on the disc samples. The anode images were collected by means of a 20 kV acceleration beam voltage and a working distance (WD) of 18.5 mm. Cathode images were acquired with a 20 kV acceleration beam voltage and a working distance (WD) of 16.0 mm. The Energy Disperse X-ray Analysis (EDX) spectra were collected at 20 kV on a 0.8 mm² area. To analyze the cross-section and measure the thickness electrodes, a small piece of sample was incorporated into a resin block that was successively polished and metalized using Ag.

2.6. Particle Size Analysis

NMC811 electrodes were composed by particles of active material dispersed in a polyvinylidene fluoride (PVDF) based binder matrix. Since the distribution of the particles dimension is a useful parameter to follow the aging, the progressive active material particles' disaggregation was checked and compared with the BOL (beginning of life) cell condition. An Antopaar 1090 PSA instrument was used to analyze NMC811 cathode particles materials.

The analysis was performed using a particle size analyzer based on the static light scattering principle. A laser beam was scattered by the dispersed particles sample and the intensity of light scattered was linked to the particles' diameter. The dispersion has been performed in a liquid medium (water).

For cathodic materials, the analysis was performed in liquid dispersion to properly spread the particles. Before starting the test, it was necessary to remove the PVDF. NMC811 electrode samples was treated at high temperature (350 °C for 1 h) and then the active material was detached from the Al current collector surface.

The analysis was performed without ultrasound dispersion to avoid further particles' disaggregation. The pump and the stirring were set at a high velocity (250 rpm), repeating the test five times, to assess the stability and the reproducibility of the measurement. The particle size distribution was estimated through the Fraunhofer diffraction equation, which predicts the angular location of the scatter maxima and minima as a function of an object's size.

2.7. ICP-OES Analysis

For the quantification of the cathode composition, an inductively coupled plasma (ICP) analysis was performed on calcined cathode powder (350 °C—1 h). A total of 0.25 g of powder was weighed on an analytical balance (accuracy 0.0001 g), transferred to a volumetric flask (250 mL), and digested with a hot aqua regia solution on a hot plate; nickel, manganese, cobalt, and lithium were quantified using a method with three calibrated points (0 ppm, 25 ppm, 50 ppm).

2.8. Lab Scale Cells Preparation and Electrochemical Performances Tests

2.8.1. Samples Dismantling Procedure

To deeply understand the aging conditions, it was decided to dismantle the original 18650 cell and to select several disks to assemble a lab scale three-electrode cell (Pat cell form EL-Cell®, Hamburg, Germany) with 18 mm diameter cathode and anode samples.

To be sure to guarantee appropriate electric contact, it was necessary to remove the coating from one side to expose the current collector and close the electric circuit.

Electrode disks were washed using DMC (dimethyl carbonate).

Three-electrode cells were assembled in an MBraun glove box.

2.8.2. Samples Selection

Ten samples from each foil were cut and preserved in a box. The cutting of the 18 mm diameter disks was performed by selecting sample areas with no apparent damage or significant lithium plating. It was difficult to use damaged areas to build new lab scale cells, thus they were used only for other characterization techniques.

To avoid preferential samples, three electrode lab scale cells (EL Cell setup, Hamburg, Germany) were assembled by selecting random electrode disks from the prepared samples.

2.8.3. Lab Scale Cell Building

A lithium pseudo-reference electrode was inserted in the cell to measure the anodic (Si-C vs. lithium) and the full cell potential. Cathodic potential was evaluated by difference. After assembling, cells were cycled at C/10 for the formation and then to check the residual capacity.

A C/50 charge-discharge cycle (2.5–4.2 V) was applied to calculate the incremental capacity analysis in three electrode conditions at a quasi-stationary state [35].

3. Results

3.1. Cycle Aging Campaing

Figure 3 shows the aging trend displayed as SoH % as a function of the number of cycles for five 18650 cylindrical cells. Each cell was aged with a specific DCFC profile, tuned and selected as shown in a previous work [11], where several cells from other cycling campaigns were already aged up to 300 cycles with good reproducibility. At Figure S1, supporting information is visible on the updated trend up to 500 cycles of a previous aging campaign, confirming the reproducibility of experimental results.
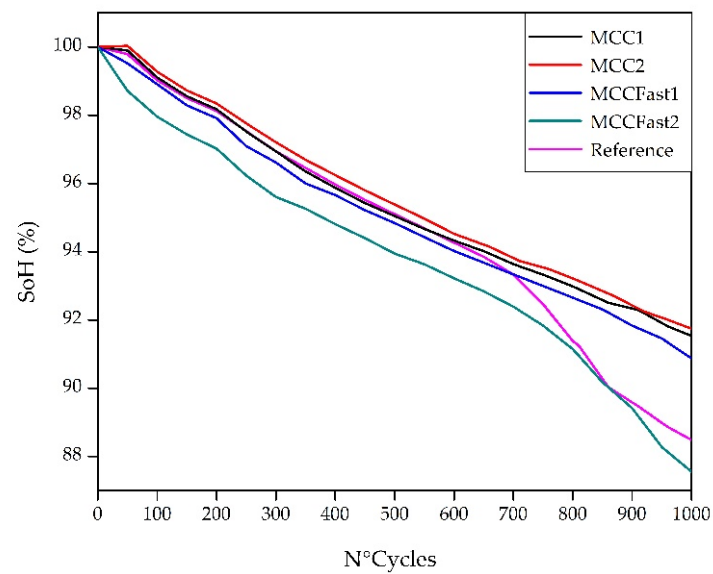
Figure 3. Cycle aging campaign SoH(%) vs. n° cycles.

3.2. Non-Disruptive Characterization Techniques

Figure 4 shows the ICA analysis performed on reference and MCC2 profile cells, both at the beginning of life (BOL) and EOL conditions. See supporting information (Figure S2) for the complete comparison. Further details will be provided in Section 4.2.
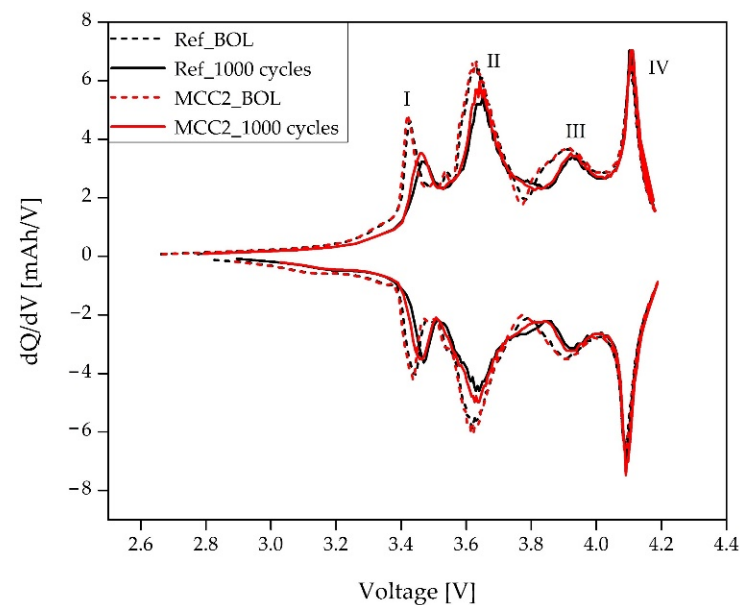

Figure 4. Incremental capacity analysis at BOL and EOL conditions.

Figure 5 shows a comparison between internal resistance (R_{int}) characterization performed on a fresh 18650 cell (Figure 5a), and two aged cells. Details about the methodology were discussed in a previous work [11].
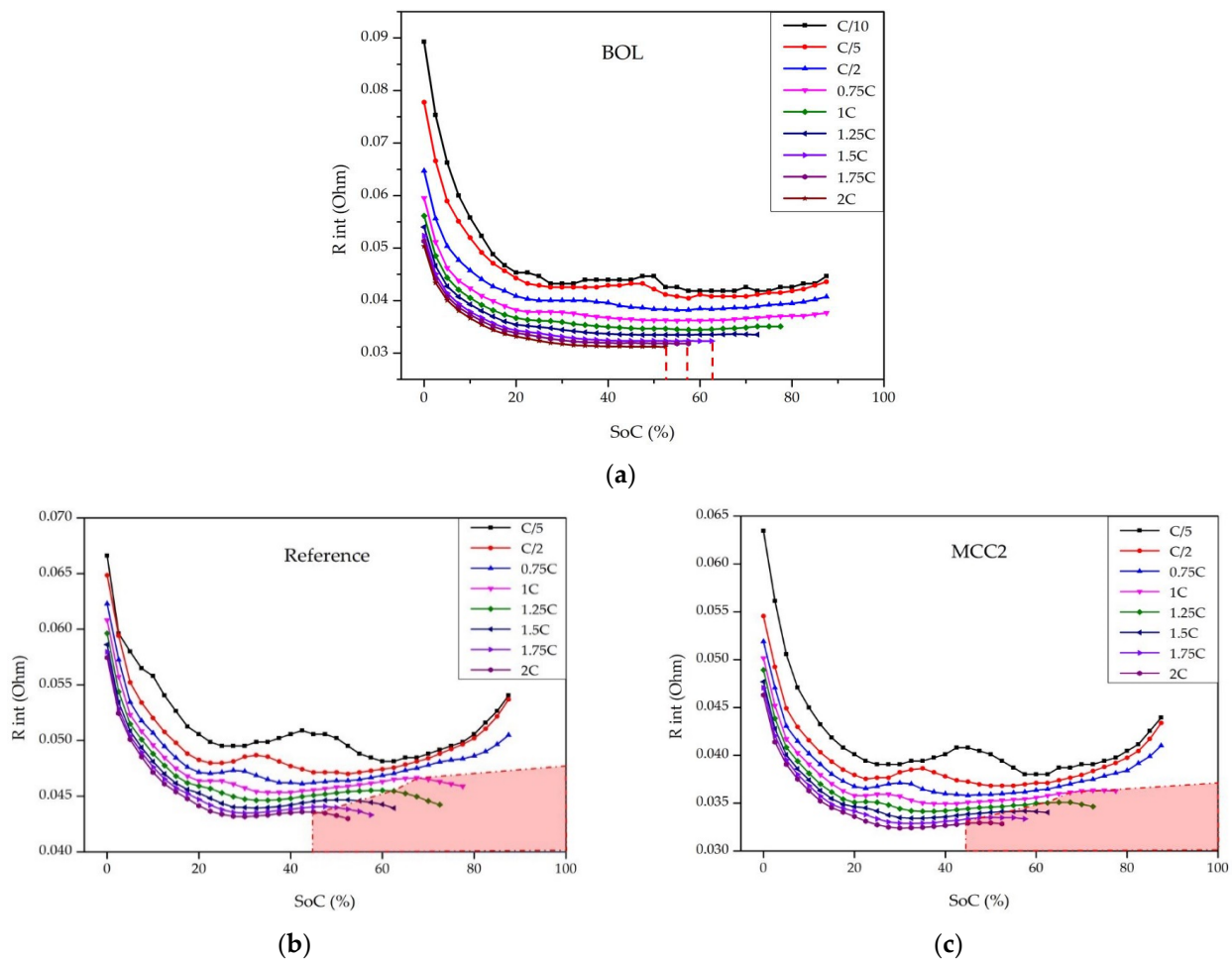
(**a**)

(**b**)																					(**c**)

Figure 5. Internal resistance trend as a function of SoC (%) for (**a**) BOL cell; (**b**) Reference EOL cell; (**c**) MCC2 EOL cell.

Figure 5b,c shows the internal resistance evolution as a function of SoC% for the reference and MCC2 profile cells. The plating zone, if present, is marked with a red area. The complete absence of lithium plating conditions for the BOL cell is visible. On the contrary, the red area is present for EOL conditions. Further details will be provided in Section 4.2.

3.3. Disruptive Characterization Techniques

3.3.1. Visual Inspection

After the dismantling of the cells, photography images were collected on all the samples (Figures S3–S7 on supporting information). Figure 6 shows details on anode electrode foils for all the implemented DCFC profiles samples. A visible lithium plating zone is present for samples subjected to reference and MCCFast2 DCFC cycling conditions, marked with a red arrow.

Figure 6. Photo images from anode samples, after 1000 cycles.

3.3.2. Scanning Electron Microscopy, ICP-OES, and Particle Size Analysis

Figure 7a,b shows, respectively, the SEM images of the reference DCFC profile anode and cathode surface. Figure 7a depicts a wide area of lithium plating depositions (red zone). Where lithium deposits are absent, it is possible to notice the graphite, even if the typical flake structure was not observable at this magnification.

Figure 7b shows the NMC811 cathode surface. The particles appear severely damaged, with a diffused particle cracking and the important presence of disaggregated particles, as stated in the literature [36].

Figure 7c shows a detail from an MCCFast2 DCFC profile, where particles with no severe damage are also observable, notwithstanding the severity of the applied charging profile.

More images on the cathode side are available in the Supporting Information (Figure S8).

ICP-OES analysis performed on cathode samples confirm no significant damage. The transition metal ratio (Ni:Mn:Co) remains unchanged after 1000 cycles with respect to the BOL cell conditions.

Figure 7d resumes the particle size analysis performed on NMC811 cathodes in all of the tested DCFC conditions, comparing the particle size distribution with a cell in fresh conditions, with no cycle aging.
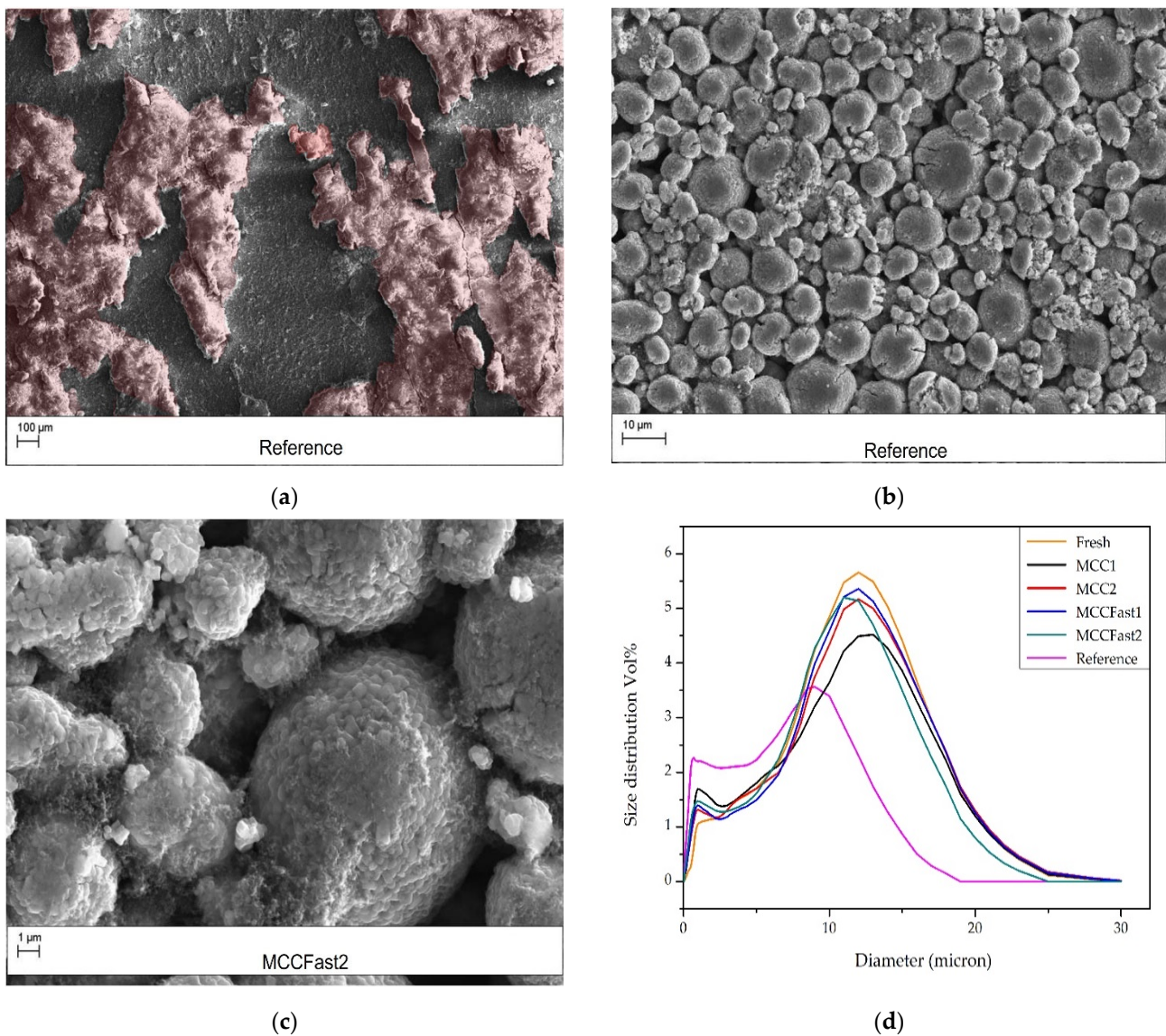
(**a**)

(**b**)

(**c**)

(**d**)

Figure 7. SEM pictures of: (**a**) Reference anode sample; (**b**) Reference cathode sample; (**c**) MCCFast2 cathode sample; (**d**) Particle size distribution on cathode particles after different charging protocols.

3.3.3. Three Electrode Lab Scale Cell–Incremental Capacity Analysis

Three electrode lab scale cells for all tested DCFC conditions were assembled to highlight the Si-C and NMC811 aging conditions by using a lithium pseudo reference electrode. In Figure 8, reference and MCC2 cells after 1000 cycles are displayed, with the fresh cell conditions (BOL) reported for comparison. More information is available in the Supporting Information (Figure S9).
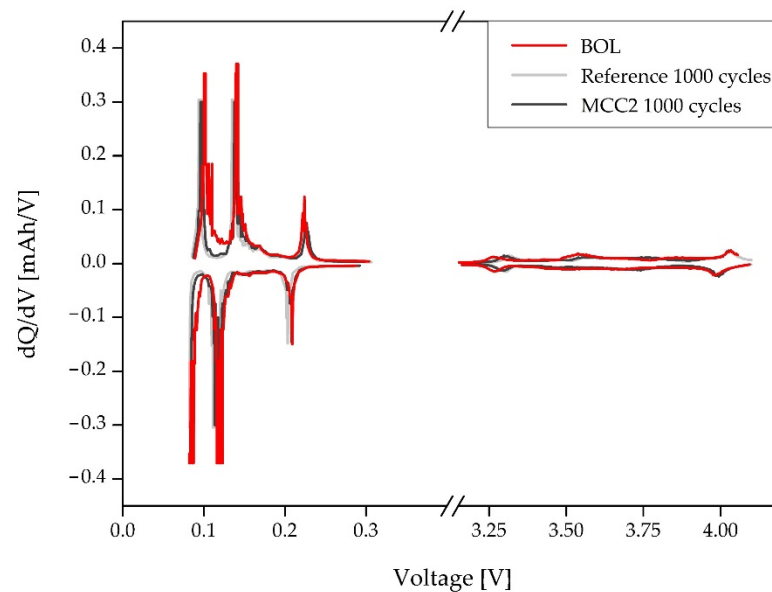
Figure 8. Three electrode incremental capacity analysis.

3.3.4. X-ray Diffraction Analysis

Table 1 summarizes the results obtained by the Rietveld refinement performed on NMC 811 cathode powders samples, in all the tested DCFC conditions. It is visible:

- Low a (Å) lattice parameter values for the most aged cells (Reference and MCCFast2);
- High c (Å) lattice parameter values for the most aged cells (Reference and MCCFast2);
- Absence of Li/Ni mixing.

Table 1. Rietveld refinement parameters.

	Lattice Parameters from the Rietveld Refinement for EOL 1000 Cycles Cells				
	Reference	**MCC1**	**MCC2**	**MCCFast1**	**MCCFast2**
a (Å)	2.867	2.871	2.870	2.870	2.868
c (Å)	14.258	14.252	14.249	14.252	14.257
I_{003}/I_{104}	1.49	1.54	1.59	1.54	1.53

4. Discussion

4.1. Cycle Aging Campaign

The SoH trend vs. n° cycles (Figure 3) showed a linear trend for MCC1, MCC2, and MCCFast1 samples. The MCCFast2 and the reference showed the worst performances, with a significant change in the trend at approximately cycle n° 700. In accordance with the literature [22,23,34,37], the pronounced change in the SoH capacity trend shown by MCCFast2 and reference samples indicate the beginning of the irreversible lithium plating phenomenon, with the concurrent loss of cyclable lithium. MCCFast2, even if started with the worst capacity retention, arrived at 1000 cycles with a capacity loss comparable to the reference profile.

As expected, MCC1 and MCC2 DCFC samples presented the best improved capacity retention, during the entire duration of the test, with respect to the reference.

4.2. Non-Disruptive Characterization Techniques

4.2.1. Incremental Capacity Analysis (ICA) on Full 18650 Cells

All the ICA trends visible in Figure 4 highlighted the transition phases coming from the full 18650 cells, with contributions coming from both the Si-C anode and the NMC 811 cathode [32,38,39]. Considering one of the displayed curves from the plot, it is possible to

identify a peak around 3.4 V, related to the lithiation (lithium intercalation) of the graphite ($C_6 \rightarrow LiC_x$). From 3.6 and 4.1 V, there is a group of three main peaks, all attributed to the NMC 811 transition phases, respectively, $H_1 \rightarrow M$ (3.6 V), $M \rightarrow H_2$ (3.9 V), and $H_2 \rightarrow H_3$ (4.1 V). Peaks at 3.9 V and 4.1 V are characteristics of high Ni-content NMCs (Ni > 80%) [40]. The peak at 3.6 V indicates the transition phase $H_1 \rightarrow M$ (first hexagonal to monoclinic); at 3.9 V it is possible to notice the $M \rightarrow H_2$ (monoclinic to second hexagonal); and, at 4.1 V, the $H_2 \rightarrow H_3$ transition phase (second to third hexagonal phase transition). The damaging effect of the transition $H_2 \rightarrow H_3$ is known from the literature because of a significant volume contraction linked to capacity fade [40–42].

Having a look at the dQ/dV vs. V trend in Figure 4, both reference and MCC2 samples show, after 1000 cycles, a general peak shift to higher voltages of the aged materials with respect to BOL. This behavior is indicative of a resistance growth. Cycle aging induced a concurrent shift and area reduction of the peaks from I to III of both 1000 cycles samples. The reference sample showed a more pronounced aging effect. The first peak (3.4 V) appears the most shifted and reduced because of the capacity loss, due to electrolyte and lithium losses, to form SEI (solid electrolyte interphase). The second (3.6 V) and the third (3.9 V) peaks exhibit an area decrease, in line with a general capacity loss, along with a small shift due to resistance increase. No evident changes in the initial crystal structure are visible since we do not observe any disappearance of peaks. Peak IV ($H_2 \rightarrow H_3$ phase transition) seems to be unaltered at 1000 cycles, with a good reversibility of the transition phase and no detrimental lattice shrinkage along the c-direction [43].

The obtained results are in accordance with the expectations, since the main purpose of the present work was to limit aging by tuning the DCFC step properly. Incremental capacity analysis confirmed a very limited aging trend from the cathode point of view, for the entire cycle aging campaign.

4.2.2. Internal Resistance Evolution

The plating zone in both cases (Figure 5) is depicted by a red area. Having a look at the BOL conditions, we can notice the total lack of plating evolution even at the highest C rates, within the limits of the test performed, as confirmed by the literature [44].

It is possible to see how, even if the current applied to the aged cells was reduced based on the measured capacity (after 1000 cycles), the inversion in the slope of the internal resistance trend at the highest C-rates (above 1C) takes place at low SoCs, if compared to the BOL conditions. See Supporting Information (Figure S10) for the complete comparison.

As expected, a simple reduction of the current based on the measured capacity (Ah) is not enough to develop a derating function. To prevent irreversible lithium plating formation, a change in the cut-off voltage (or alternatively a more pronounced current reduction) is needed to protect the cells over their lifetime.

4.3. Disruptive Characterization Techniques

4.3.1. Visual Inspection

Figure 6 shows the visual inspection of the Si-C anodes both from the dismantling of the MCC1, MCC2, MCCFast1, MCCFast2, and reference cells, after 1000 cycles. It is visible how the anode surface seems to be totally unaltered for MCC1 and MCC2 samples, except for a very small portion of the electrode affected by lithium plating, in the case of MCC2.

MCCFast1 shows a yellow zone, attributable to an initial lithium plating, even if in small quantities.
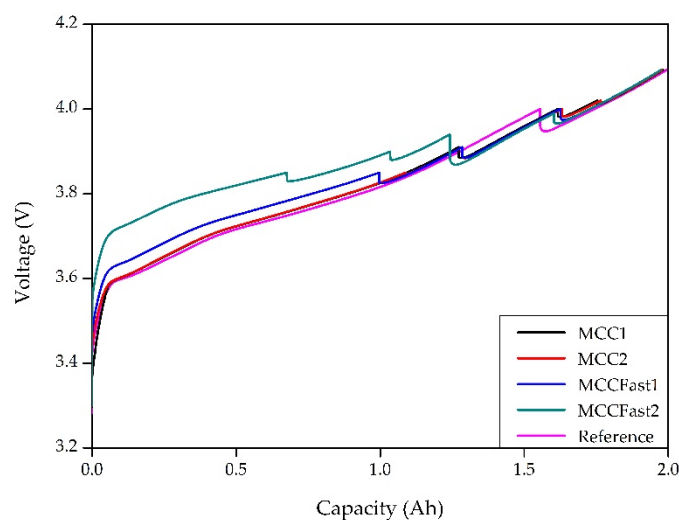
MCCFast2 and reference anodes present a significant amount of lithium deposition on both sides of the electrode (about 10×3 cm^2). Images (Figure 6) are in good accordance with the electrical results summarized in Table 2, where it is possible to appreciate the SoH%, at the end of the cycling campaign.

Table 2. Final SoH% values for the implemented DCFC profiles.

	Reference	**MCC1**	**MCC2**	**MCCFast1**	**MCCFast2**
SoH %	88.48	91.53%	91.74%	90.88%	87.55%

The presence of lithium deposits in the inner rolls of the cell, where present, indicates the concurrent effect of the high current applied (crucial effect when the cell aged) and a geometrical influence [45–47]. In fact, the pressure applied on the electrode foils increases by going from the outer to the inner layers, with a direct influence of a thick element useful to link and wrap the two parts of each electrode and separator foil. See Supporting Information (Figures S3–S7, yellow element).

Having a look at the charging profile (Figure 9) we can see how MCCFast2 profile restores the highest amount of capacity (Ah) in the first 15 min, 20% more than with the reference, as reported in Table 3.

Figure 9. Voltage response in function of the capacity for the implemented DCFC profiles.

Table 3. Time table for the charging step.

Time for Charge [Minute]	5	10	15	20	25	30
Reference	16%	25%	33%	41%	50%	58%
MCC1	16%	25%	35%	44%	53%	60%
MCC2	17%	26%	35%	44%	53%	60%
MCCFast1	19%	30%	41%	50%	58%	64%
MCCFast2	25%	40%	**53%**	59%	65%	70%

Because of the obtained results, we can affirm that this profile can be ideal to fast charge (under 30 min) the battery pack when needed, permitting, among the selected profiles, the highest energy throughput in the lowest amount of time. On the contrary, the reference DCFC profile, which aged more in comparison to the other faster DCFC profiles, also restores the lowest amount of energy after 30 min, with no evident advantages in the application. On the contrary, MCCFast2 results in an effective approach for occasional charging.

4.3.2. SEM, ICP-OES, and Particle Size Analysis

In Figure 7a, where the lithium plating is absent, it was expected to see the presence of the graphite structure, which seems to be covered by a uniform layer. The main hypothesis is relative to a thick SEI layer presence all over the electrode.

From Figure 7b we can assume that the reference DCFC condition caused more mechanical stress inside the NMC811 particles, if compared to the MCCFast2 condition, as seen in Figure 7c.

Even though the higher C-rates applied during the first steps of the charging profile, MCCFast2 seems to be a valid alternative to the reference. From a general aging point of view, the results are very similar, with the main difference in the cathode particle cracking point of view. It seems that currents used inside the MCCFast2 profile, permit a better Li^+ diffusion inside the cathode particles, preventing the formation of cracks [36].

Figure 7d reports the particle size distribution of NMC811 in all the tested conditions. From a statistical point of view, all the implemented DCFC profiles seem to be able to maintain the average particle distribution reported at BOL stage, where the cell did not undergo cycle aging.

Reference DCFC profile shows the worst case condition from the particle size distribution point of view, with the decrease of the main peak (around 10 μm) and a concurrent shift towards smaller diameters. The increasing of a particles' family at smaller diameters (around 1 μm) is also observable, data that is in accordance with the severe cracking observed with the SEM analysis and a result that is in line with other works [48,49].

4.3.3. Three-Electrode Lab Scale Cell—ICA

Figure 8 shows MCC2 and reference samples in both anode and cathode voltage profiles, together with the BOL cell sample.

It is possible to notice the general good health of the selected samples (see Material and Methods for details).

Incremental capacity analysis on a three-electrode lab scale cell does not reveal significant damage inside the cell, where no lithium plating was observed at the visual inspection.

Looking at the peaks in both anode (Si-C vs. Li) and cathode (NMC811 vs. Li) voltage trends, a good matching in term of peak position, between EOL and BOL cell samples, was also found. This behavior is indicative of no significant resistance growth inside the cells assembled with the selected samples. We can observe a general decrease of the peak values with respect to the BOL cell, indicating an expected capacity loss due to normal aging.

When lithium plating is present [34], a significant peak shift and area (below the ICA curve) reduction was observed in the anodic voltage response.

Both MCC2 and reference EOL curves are close to be overlapped (conversely to the overall ICA response on 18650 cells at Figure 4), suggesting that localized lithium plating is the driving aging phenomenon of the performed cycle aging campaign.

4.3.4. XRD Measurements

Data collected on cathode samples in both powders and calendered conditions do not present significant differences from the XRD pattern point of view (see Supporting Information (Figure S11)).

NMC811 material maintained the initial hexagonal crystal structure ($R\bar{3}m$ space group).

From the Rietveld refinement (Figure S12 in Supporting Information) performed on cathode powders, it was possible to measure the evolution of the crystal lattice parameters a and c. As confirmed by the literature [31,50], aging mechanisms inside the Li-ion cell induce a shrinkage of the lattice along a-axis and a concurrent stretching along c-axis.

The main hypothesis of this behavior is attributable to:

The increase of repulsive forces between slabs due to the decrease of the lithium content in the EOL electrode materials [27,51];

The increase of the average oxidation state for nickel, manganese, and cobalt ions [52].

Cathode peak intensity ratio performed on 003 and 104 peaks (Figure S12) was measured to evaluate the presence of cation mixing. It is known from the literature [53,54] how the relative ratio of the intensities I_{003}/I_{104} is associated to the presence of this phenomenon, visible in Table 1. Values below 1.2 are indicative of significant aging.

From the data collected for the present work, all the values are above 1.49, indicative of the lack of cation mixing.

Lattice parameter evolution and cation mixing absence are a clear sign of the general good health of the tested materials, confirming that the main aging mechanism in our testing conditions is lithium plating, localized only to small portions of the electrode foil.

5. Conclusions

The present work presented data and results obtained from a cycle aging campaign performed on 18650 cells, aged using four new implemented custom designed DCFC profiles, and compared to a reference condition. It was seen how some of the new conditions could provide better behavior in terms of aging and time saving (especially for MCCFast2). Among the main results it is possible to state that:

- The use of ICA in the present study confirms the general good health of the tested cells, indeed no significant degradation on the NMC811 electrode was observed and localized degradation on the Si-C electrode, where lithium plating occurs, was noticed. Physicochemical characterization, along with visual inspection, confirms data obtained from ICA, both in full cells and in lab scale three-electrode cells. Where no evident damage is visible on the electrode samples, ICA responses confirm the absence of significant degradation;

- Among the new implemented approaches, internal resistance test (R_{int} vs. SoH%) can be considered as a useful "in situ" methodology to control the current (and voltage) limits on the cell, during the aging cycle.

It was observed how the implementation of a derating function, based only on the reduction of cell capacity over a lifetime, was not exhaustive for avoiding a lithium plating phenomenon. This technique seems to be promising to tune the charging steps continuously, by performing a period check on the battery system. Since it does not require complex instrumentation, it presents a concrete possibility to be implemented as an "on board" application on BMS.

Data Availability Statement: Not applicable.

Conflicts of Interest: The authors declare no conflict of interest.

Abbreviations

MCC	Multistage Constant Current
Ref	Reference
SEM	Scanning Electron Microscopy
XRD	X-Ray Diffraction
ICE	Internal Combustion Engine
BMS	Battery Management System
DoD	Depth of Discharge
LLI	Loss of Lithium Inventory
SEI	Solid Electrolyte Interphase
LAM	Loss of Active Material
ORI	Ohmic Resistance Increase
SoH	State of Health
ICA	Incremental Capacity Analysis
EC:DMC	Ethylen carbonate:Dymethyl carbonate
$LiPF_6$	Lithium exafluorophosfate
DCFC	Direct Current Fast Charging
EOL	End of Life
C-rate	Charging rate
SoD	State of Discharge
WD	Working Distance
EDX	Energy Dispersive X-Ray Analysis

References

1. Abraham, K.M. How Comparable Are Sodium-Ion Batteries to Lithium-Ion Counterparts? *ACS Energy Lett.* **2020**, *5*, 3544–3547. [CrossRef]
2. Li, C.; Wang, Z.; He, Z.; Li, Y.; Mao, J.; Dai, K.; Yan, C.; Zheng, J. An Advance Review of Solid-State Battery: Challenges, Progress and Prospects. *Sustain. Mater. Technol.* **2021**, *29*, e00297. [CrossRef]
3. Kwak, W.-J.; Rosy; Sharon, D.; Xia, C.; Kim, H.; Johnson, L.R.; Bruce, P.G.; Nazar, L.F.; Sun, Y.-K.; Frimer, A.A.; et al. Lithium–Oxygen Batteries and Related Systems: Potential, Status, and Future. *Chem. Rev.* **2020**, *120*, 6626–6683. [CrossRef] [PubMed]
4. Sun, K.; Peng, Z. Intermetallic Interphases in Lithium Metal and Lithium Ion Batteries. *InfoMat* **2021**, *3*, 1083–1109. [CrossRef]
5. Li, S.; Leng, D.; Li, W.; Qie, L.; Dong, Z.; Cheng, Z.; Fan, Z. Recent Progress in Developing Li2S Cathodes for Li–S Batteries. *Energy Storage Mater.* **2020**, *27*, 279–296. [CrossRef]
6. Ahniyaz, A.; de Meatza, I.; Kvasha, A.; Garcia-Calvo, O.; Ahmed, I.; Sgroi, M.F.; Giuliano, M.; Dotoli, M.; Dumitrescu, M.-A.; Jahn, M.; et al. Progress in Solid-State High Voltage Lithium-Ion Battery Electrolytes. *Adv. Appl. Energy* **2021**, *4*, 100070. [CrossRef]
7. Armand, M.; Axmann, P.; Bresser, D.; Copley, M.; Edström, K.; Ekberg, C.; Guyomard, D.; Lestriez, B.; Novák, P.; Petranikova, M.; et al. Lithium-Ion Batteries—Current State of the Art and Anticipated Developments. *J. Power Sources* **2020**, *479*, 228708. [CrossRef]
8. Ding, Y.; Cano, Z.P.; Yu, A.; Lu, J.; Chen, Z. Automotive Li-Ion Batteries: Current Status and Future Perspectives. *Electrochem. Energy Rev.* **2019**, *2*, 1–28. [CrossRef]
9. Opitz, A.; Badami, P.; Shen, L.; Vignarooban, K.; Kannan, A.M. Can Li-Ion Batteries Be the Panacea for Automotive Applications? *Renew. Sustain. Energy Rev.* **2017**, *68*, 685–692. [CrossRef]
10. Li, J.; Du, Z.; Ruther, R.E.; An, S.J.; David, L.A.; Hays, K.; Wood, M.; Phillip, N.D.; Sheng, Y.; Mao, C.; et al. Toward Low-Cost, High-Energy Density, and High-Power Density Lithium-Ion Batteries. *JOM* **2017**, *69*, 1484–1496. [CrossRef]
11. Dotoli, M.; Milo, E.; Giuliano, M.; Rocca, R.; Nervi, C.; Baricco, M.; Ercole, M.; Sgroi, M.F. Detection of Lithium Plating in Li-Ion Cell Anodes Using Realistic Automotive Fast-Charge Profiles. *Batteries* **2021**, *7*, 46. [CrossRef]
12. Epding, B.; Rumberg, B.; Mense, M.; Jahnke, H.; Kwade, A. Aging—Optimized Fast Charging of Lithium Ion Cells Based on Three-Electrode Cell Measurements. *Energy Technol.* **2020**, *8*, 2000457. [CrossRef]
13. Atalay, S.; Sheikh, M.; Mariani, A.; Merla, Y.; Bower, E.; Widanage, W.D. Theory of Battery Ageing in a Lithium-Ion Battery: Capacity Fade, Nonlinear Ageing and Lifetime Prediction. *J. Power Sources* **2020**, *478*, 229026. [CrossRef]
14. Barré, A.; Deguilhem, B.; Grolleau, S.; Gérard, M.; Suard, F.; Riu, D. A Review on Lithium-Ion Battery Ageing Mechanisms and Estimations for Automotive Applications. *J. Power Sources* **2013**, *241*, 680–689. [CrossRef]

15. Schlasza, C.; Ostertag, P.; Chrenko, D.; Kriesten, R.; Bouquain, D. Review on the Aging Mechanisms in Li-Ion Batteries for Electric Vehicles Based on the FMEA Method. In Proceedings of the 2014 IEEE Transportation Electrification Conference and Expo (ITEC), Dearborn, MI, USA, 15–18 June 2014; pp. 1–6.

16. Lin, C.; Tang, A.; Mu, H.; Wang, W.; Wang, C. Aging Mechanisms of Electrode Materials in Lithium-Ion Batteries for Electric Vehicles. *J. Chem.* **2015**, *2015*, 104673. [CrossRef]

17. Xiong, R.; Pan, Y.; Shen, W.; Li, H.; Sun, F. Lithium-Ion Battery Aging Mechanisms and Diagnosis Method for Automotive Applications: Recent Advances and Perspectives. *Renew. Sustain. Energy Rev.* **2020**, *131*, 110048. [CrossRef]

18. Essl, C.; Seifert, L.; Rabe, M.; Fuchs, A. Early Detection of Failing Automotive Batteries Using Gas Sensors. *Batteries* **2021**, *7*, 25. [CrossRef]

19. Birkl, C.R.; Roberts, M.R.; McTurk, E.; Bruce, P.G.; Howey, D.A. Degradation Diagnostics for Lithium Ion Cells. *J. Power Sources* **2017**, *341*, 373–386. [CrossRef]

20. Koleti, U.R.; Rajan, A.; Tan, C.; Moharana, S.; Dinh, T.Q.; Marco, J. A Study on the Influence of Lithium Plating on Battery Degradation. *Energies* **2020**, *13*, 3458. [CrossRef]

21. Agubra, V.; Fergus, J. Lithium Ion Battery Anode Aging Mechanisms. *Materials* **2013**, *6*, 1310–1325. [CrossRef]

22. Keil, J.; Paul, N.; Baran, V.; Keil, P.; Gilles, R.; Jossen, A. Linear and Nonlinear Aging of Lithium-Ion Cells Investigated by Electrochemical Analysis and In-Situ Neutron Diffraction. *J. Electrochem. Soc.* **2019**, *166*, A3908–A3917. [CrossRef]

23. Diao, W.; Saxena, S.; Han, B.; Pecht, M. Algorithm to Determine the Knee Point on Capacity Fade Curves of Lithium-Ion Cells. *Energies* **2019**, *12*, 2910. [CrossRef]

24. Schuster, S.F.; Bach, T.; Fleder, E.; Müller, J.; Brand, M.; Sextl, G.; Jossen, A. Nonlinear Aging Characteristics of Lithium-Ion Cells under Different Operational Conditions. *J. Energy Storage* **2015**, *1*, 44–53. [CrossRef]

25. Waldmann, T.; Iturrondobeitia, A.; Kasper, M.; Ghanbari, N.; Aguesse, F.; Bekaert, E.; Daniel, L.; Genies, S.; Gordon, I.J.; Löble, M.W.; et al. Review—Post-Mortem Analysis of Aged Lithium-Ion Batteries: Disassembly Methodology and Physico-Chemical Analysis Techniques. *J. Electrochem. Soc.* **2016**, *163*, A2149–A2164. [CrossRef]

26. Kuntz, P.; Raccurt, O.; Azaïs, P.; Richter, K.; Waldmann, T.; Wohlfahrt-Mehrens, M.; Bardet, M.; Buzlukov, A.; Genies, S. Identification of Degradation Mechanisms by Post-Mortem Analysis for High Power and High Energy Commercial Li-Ion Cells after Electric Vehicle Aging. *Batteries* **2021**, *7*, 48. [CrossRef]

27. Buchberger, I.; Seidlmayer, S.; Pokharel, A.; Piana, M.; Hattendorff, J.; Kudejova, P.; Gilles, R.; Gasteiger, H.A. Aging Analysis of Graphite/LiNi$_{1/3}$ Mn$_{1/3}$ Co$_{1/3}$ O$_2$ Cells Using XRD, PGAA, and AC Impedance. *J. Electrochem. Soc.* **2015**, *162*, A2737–A2746. [CrossRef]

28. Tian, Y.; Lin, C.; Li, H.; Du, J.; Xiong, R. Detecting Undesired Lithium Plating on Anodes for Lithium-Ion Batteries—A Review on the in-Situ Methods. *Appl. Energy* **2021**, *300*, 117386. [CrossRef]

29. Schindler, S.; Bauer, M.; Petzl, M.; Danzer, M.A. Voltage Relaxation and Impedance Spectroscopy as In-Operando Methods for the Detection of Lithium Plating on Graphitic Anodes in Commercial Lithium-Ion Cells. *J. Power Sources* **2016**, *304*, 170–180. [CrossRef]

30. Janakiraman, U.; Garrick, T.R.; Fortier, M.E. Review—Lithium Plating Detection Methods in Li-Ion Batteries. *J. Electrochem. Soc.* **2020**, *167*, 160552. [CrossRef]

31. Dotoli, M.; Rocca, R.; Giuliano, M.; Sgroi, M.; Belforte, L.; Li Pira, N.; Mangione, G.; Milo, E.; Nicol, G.; Parussa, F. Physical-Chemical Characterization of Cycle Aged Commercial Cells of Automotive Interest. In Proceedings of the WCX SAE World Congress Experience, Detroit, MI, USA, 5–7 April 2022. SAE Technical Paper 2022-01-027.

32. Krupp, A.; Ferg, E.; Schuldt, F.; Derendorf, K.; Agert, C. Incremental Capacity Analysis as a State of Health Estimation Method for Lithium-Ion Battery Modules with Series-Connected Cells. *Batteries* **2020**, *7*, 2. [CrossRef]

33. Riviere, E.; Sari, A.; Venet, P.; Meniere, F.; Bultel, Y. Innovative Incremental Capacity Analysis Implementation for C/LiFePO4 Cell State-of-Health Estimation in Electrical Vehicles. *Batteries* **2019**, *5*, 37. [CrossRef]

34. Bach, T.C.; Schuster, S.F.; Fleder, E.; Müller, J.; Brand, M.J.; Lorrmann, H.; Jossen, A.; Sextl, G. Nonlinear Aging of Cylindrical Lithium-Ion Cells Linked to Heterogeneous Compression. *J. Energy Storage* **2016**, *5*, 212–223. [CrossRef]

35. Fly, A.; Chen, R. Rate Dependency of Incremental Capacity Analysis (DQ/DV) as a Diagnostic Tool for Lithium-Ion Batteries. *J. Energy Storage* **2020**, *29*, 101329. [CrossRef]

36. Christensen, J.; Newman, J. A Mathematical Model of Stress Generation and Fracture in Lithium Manganese Oxide. *J. Electrochem. Soc.* **2006**, *153*, A1019. [CrossRef]

37. Kalaga, K.; Rodrigues, M.-T.F.; Trask, S.E.; Shkrob, I.A.; Abraham, D.P. Calendar-Life versus Cycle-Life Aging of Lithium-Ion Cells with Silicon-Graphite Composite Electrodes. *Electrochim. Acta* **2018**, *280*, 221–228. [CrossRef]

38. Chen, Y.; Torres-Castro, L.; Chen, K.-H.; Penley, D.; Lamb, J.; Karulkar, M.; Dasgupta, N.P. Operando Detection of Li Plating during Fast Charging of Li-Ion Batteries Using Incremental Capacity Analysis. *J. Power Sources* **2022**, *539*, 231601. [CrossRef]

39. Plattard, T.; Barnel, N.; Assaud, L.; Franger, S.; Duffault, J.-M. Combining a Fatigue Model and an Incremental Capacity Analysis on a Commercial NMC/Graphite Cell under Constant Current Cycling with and without Calendar Aging. *Batteries* **2019**, *5*, 36. [CrossRef]

40. Jung, R.; Metzger, M.; Maglia, F.; Stinner, C.; Gasteiger, H.A. Oxygen Release and Its Effect on the Cycling Stability of LiNi x Mn y Co z O 2 (NMC) Cathode Materials for Li-Ion Batteries. *J. Electrochem. Soc.* **2017**, *164*, A1361–A1377. [CrossRef]

41. de Biasi, L.; Schwarz, B.; Brezesinski, T.; Hartmann, P.; Janek, J.; Ehrenberg, H. Chemical, Structural, and Electronic Aspects of Formation and Degradation Behavior on Different Length Scales of Ni-Rich NCM and Li-Rich HE-NCM Cathode Materials in Li-Ion Batteries. *Adv. Mater.* **2019**, *31*, 1900985. [CrossRef]

42. Li, T.; Yuan, X.-Z.; Zhang, L.; Song, D.; Shi, K.; Bock, C. Degradation Mechanisms and Mitigation Strategies of Nickel-Rich NMC-Based Lithium-Ion Batteries. Electrochem. *Energy Rev.* **2020**, *3*, 43–80. [CrossRef]

43. Jung, S.-K.; Gwon, H.; Hong, J.; Park, K.-Y.; Seo, D.-H.; Kim, H.; Hyun, J.; Yang, W.; Kang, K. Understanding the Degradation Mechanisms of LiNi 0.5 Co 0.2 Mn 0.3 O 2 Cathode Material in Lithium Ion Batteries. Adv. *Energy Mater.* **2014**, *4*, 1300787. [CrossRef]

44. Cho, I.-H.; Lee, P.-Y.; Kim, J.-H. Analysis of the Effect of the Variable Charging Current Control Method on Cycle Life of Li-Ion Batteries. *Energies* **2019**, *12*, 3023. [CrossRef]

45. Sieg, J.; Bandlow, J.; Mitsch, T.; Dragicevic, D.; Materna, T.; Spier, B.; Witzenhausen, H.; Ecker, M.; Sauer, D.U. Fast Charging of an Electric Vehicle Lithium-Ion Battery at the Limit of the Lithium Deposition Process. *J. Power Sources* **2019**, *427*, 260–270. [CrossRef]

46. Rodrigues, M.T.F.; Son, S.-B.; Colclasure, A.M.; Shkrob, I.A.; Trask, S.E.; Bloom, I.D.; Abraham, D.P. How Fast Can a Li-Ion Battery Be Charged? Determination of Limiting Fast Charging Conditions. *ACS Appl. Energy Mater.* **2021**, *4*, 1063–1068. [CrossRef]

47. Baker, D.R.; Verbrugge, M.W. Modeling Overcharge at Graphite Electrodes: Plating and Dissolution of Lithium. *J. Electrochem. Soc.* **2020**, *167*, 013504. [CrossRef]

48. Sun, G.; Sui, T.; Song, B.; Zheng, H.; Lu, L.; Korsunsky, A.M. On the Fragmentation of Active Material Secondary Particles in Lithium Ion Battery Cathodes Induced by Charge Cycling. *Extrem. Mech. Lett.* **2016**, *9*, 449–458. [CrossRef]

49. Aishova, A.; Park, G.; Yoon, C.S.; Sun, Y. Cobalt—Free High—Capacity Ni—Rich Layered Li[Ni$_{0.9}$ Mn$_{0.1}$]O$_2$ Cathode. *Adv. Energy Mater.* **2020**, *10*, 1903179. [CrossRef]

50. Friedrich, F.; Strehle, B.; Freiberg, A.T.S.; Kleiner, K.; Day, S.J.; Erk, C.; Piana, M.; Gasteiger, H.A. Editors' Choice—Capacity Fading Mechanisms of NCM-811 Cathodes in Lithium-Ion Batteries Studied by X-Ray Diffraction and Other Diagnostics. *J. Electrochem. Soc.* **2019**, *166*, A3760–A3774. [CrossRef]

51. Wu, X.; Bai, Y.; Li, Z.; Liu, J.; Zhao, K.; Du, Z. Effects of Charging Rates on LiNi$_{0.6}$Mn$_{0.2}$Co$_{0.2}$O$_2$ (NMC622)/Graphite Li-Ion Cells. *J. Energy Chem.* **2021**, *56*, 121–126. [CrossRef]

52. Sun, H.; Zhao, K. Electronic Structure and Comparative Properties of LiNix Mny Coz O$_2$ Cathode Materials. *J. Phys. Chem. C* **2017**, *121*, 6002–6010. [CrossRef]

53. Gupta, H.; Singh, R.K. High-Voltage Nickel—Rich NMC Cathode Material with Ionic-Liquid-Based Polymer Electrolytes for Rechargeable Lithium-Metal Batteries. *ChemElectroChem* **2020**, *7*, 3597–3605. [CrossRef]

54. Radziuk, D.; Möhwald, H. Ultrasonically Treated Liquid Interfaces for Progress in Cleaning and Separation Processes. *Phys. Chem. Chem. Phys.* **2016**, *18*, 21–46. [CrossRef] [PubMed]